Volume 15, No 1 | International Journal of Radiation Research, January 2017

Automatic detection of liver tumor motion by fluoroscopy images

H.W. Zhang[1], B. Hu[2*], Y.L. Wang[3*]

[1]*Department of Radiotherapy; Jiang-Xi Cancer Hospital; Nanchang 330029, China*
[2]*Key Laboratory of Nondestructive Testing (Ministry of Education), Nanchang Hang Kong University, Nanchang 330063, China*
[3]*Department of Radiation Oncology, PLA General Hospital, Beijing 100853, China*

► ***Original article***

Corresponding author:
Dr. Bo Hu - Dr. Y.L. Wang
Fax: *+ 48 91 4414521*
E-mail: *cumthubo@163.com*
wuming830822@163.com

Revised: April 2016
Accepted: May 2016.

Int. J. Radiat. Res., January 2017; 15(1): 49-61

DOI: 10.18869/acadpub.ijrr.15.1.49

* These authors contributed to the work equally and should be regarded as co-first authors.

ABSTRACT

Background: A method to track liver tumor motion signals from fluoroscopic images without any implanted gold fiducial markers was proposed in this study to overcome the adverse effects on precise tumor irradiation caused by respiratory movement. ***Materials and Methods***: The method was based on the following idea: (i) Before treatment, a series of fluoroscopic images corresponding to different breathing phases and tumor positions were acquired after patient set-up; (iii) The wavelet transform method and Canny edge detection algorithm were used to detect motion trajectory of the diaphragm; (iv) The motion curves of center of lipiodol in the images were obtained by mathematical morphology and median filtering algorithm. The method was evaluated using by five sequences of fluoroscopic images from TACE patients who received transcatheter arterial chemoembolization therapy. ***Results:*** The position of liver tumor was significantly affected by respiratory motion; the motion trajectories of the diaphragm and lipiodolagreed well with the manually marked locations in amplitude and period; the motion trajectories of the diaphragm and lipiodol almost had similar period and amplitude in one treatment fraction. The respiratory period and amplitude of the same patient in different fractions had no significant differences; however, the difference was obvious for different patients. The proposed lipiodol detection methods can effectively reflect the relevant rules of tumor location caused by respiratory movement. ***Conclusion:*** Direct tracking of liver tumor motion in fluoroscopic images is feasible. The automatic detection method can reflect the characteristics of respiratory and tumor motions, which can save much time and significantly improve measurement precision compared with manual measurement.

Keywords: *Respiratory movement, wavelet transform, canny edge detection algorithm, mathematical morphology, median filtering algorithm.*

INTRODUCTION

Precise radiotherapy aims to keep a high dose of planning target volume while minimizing dose to organs at risk. The therapeutic gain ratio of tumors will be maximized. Physiological and physical factors such as breathing will continue to influence the location of thoraco-abdominal tumors and organs at risk, which significantly affect the accuracy of target location and dose. Hence, a simple method is to increase the margin from clinical tumor volume (CTV) to internal target volume (ITV) to cover the possible range of target motion. However, this increase would undesirably result in an increased dose to normal tissues surrounding the tumor [1–3]. Target movement of tumors has become a bottleneck of precision radiotherapy. Thus, measuring the respiratory motion is necessary to reduce the influence of breathing movement on the location precision of the tumor target in precise radiotherapy for thoraco-abdominal

[DOI: 10.18869/acadpub.ijrr.15.1.49]

tumors. However, one of the hardest technical challenges is tracking the tumor location in real time with high precision [4].

Breath-hold and tumor tracking can effectively reduce the influence of respiration and have been widely used in treating patients with tumors in thoraco-abdominal regions [5-6]. At present, tumor tracking approaches can be roughly grouped into three categories: (1) use of external surrogates such as patient abdominal surface or lung volume to derive tumor position [7–9]; (2) tracking of implanted gold fiducial markers inside or near the tumor with fluoroscopic images [11–12]; and (3) tracking of tumor motion curve with fluoroscopic images without implanted gold fiducial markers [13–14].

The major problem of the first approach is insufficient accuracy [15]; the second approach does not have the capability of implanting the gold fiducial markers (such as standalone clinics) on all sites and has the risk of pneumothorax [16]; and the third approach is mainly ascribed to lung tumors [17]. Most marker less tracking methods have been investigated for the lungs; however, these methods are invalid for the liver because of low contrast between the tumor and healthy tissue. Therefore, new techniques for direct tracking of liver tumors without implanted markers are needed. The use of lipiodol for liver stereotactic body radiotherapy (SBRT) has the advantage of showing the liver without implanted fiducial markers. This method is sometimes used with chemotherapy, thus, patients may still undergo the procedure when undergoing radiation therapy, saving the need for an implanted fiducial. In this study, a method to track liver tumor motion signals from fluoroscopic images without any implanted gold fiducial markers was proposed in this study to overcome the adverse effects on precise tumor irradiation caused by respiratory movement. Specific content will be reported in the following parts.

MATERIALS AND METHODS

Patient selection

Four liver cancer patients who received transcatheter arterial chemoembolization therapy were eligible for inclusion in the study. All patients were male and aged 45 to 60 years, with an average of about 54.5 years old. Three cases had solitary lesion, and one case had multiple lesions. The lipiodol of the four patients was required to view the lesion and have a clear boundary. All cases had Karnofsky score of more than 70 without jaundice, ascites, or hepatic metastasis.

Image acquisition

In this study, raw real-time digital fluoroscopic images of respiratory motion for liver cancer patients in free breathing conditions was acquired using the fluoroscopy of XVI cone beam CT integrated on Elekta Synergy-S linear accelerator.XVI is an electronic imaging device that consists of a kV X-ray source, an amorphous silicon radiation image detector panel, and a computer workstation. XVI provides three modes of kV image acquisition, namely, Planar View™, Motion View™, and Volume View™. In Motion View™, a sequence of real-time planar fluoroscopic images for liver tumor tracking can be acquired. An automatic analysis of such sequences allows accurate computation of frequency and amplitude of the periodic movement under investigation. The scan voltage was 120 kV and tube current was 150 mAs. The fluoroscopic imaging duration of a treatment fraction is 150 frames. Pixel size of reconstruction matrix was 512 × 512using M20 collimator cassette (collimator with 20 cm axial field-of-view) and F0 filtration (without bowtie filter). All images were acquired in the course of treatment. To minimize the effect of set-up error on the patient's planning target volume, the patient was scanned in the Volume-View ™ mode for rigid image registration of bony structures before treatment. After treatment, the machine gantry was rotated to 90° with an error range of 0.1°. The level of CBCT kV radiation source was disposed at a position of 0°. After the radiation field was opened to the maximum, liver images were acquired using the XVI Motion-View™ image scanning mode. In XVI MotionView™, a sequence of planar images was acquired while the gantry of the linear

[DOI: 10.18869/acadpub.ijrr.15.1.49]

accelerator was static at 0°. Thus, the image sequence can show the motion of the anatomical structures within the field of view.

Image format conversion

The raw format of the fluoroscopic sequences obtained using the fluoroscopy of XVI cone beam CT was'*.his' that cannot be directly processed needs to be converted to '*.bmp' by Image J 1.46r for further processing. All the following images in this study were processed in'*.bmp' format.

Wavelet transform algorithm

The basic idea of wavelet transform is a function called the wavelet function system to represent or approximate a signal. This system constitutes 'wavelets' produced by a mother wavelet function by dilation and translation. The substance of wavelet decomposition in the image changes the image signal into different frequency components. Based on the sequence from high frequency to low frequency components, the wavelet transform decomposes an image into moultrie-solution bands. At each band is decomposed into four sub bands: approximation band AK, at the next scale, horizontal details band Hk, vertical details band Vk, and diagonal details band Dk. Four filters, namely, $h_{\Psi}(-n)$, $h_{\varphi}(-n)$, $h_{\Psi}(-m)$ and $h_{\varphi}(-n)$ were used to eliminate the noise of relatively low and relatively high frequency sequences in row and column image data. For the normal tissue, the transformed signal in the frequency domain belongs to low frequency components. By contrast, microcalcification belongs to high frequency components [18, 19]. Hence, Wk of wavelet plane can be composed by linear combination of Hk, Vk, and Dk [20]: $Wk = a|Hk| + b|Vk| + c|Dk|$, where a, b, and c are the weights of the sub-band wavelet coefficients of horizontal, vertical, and diagonal details, respectively, corresponding to the *k*th layer of wavelet plane. Therefore, different methods can be used to enhance different frequency components within the image detail, highlighting the details of different scales, thereby improving image quality. The wavelet function Sym4, from Symlets family was used to decompose and reconstruct the images in our work.

Canny edge detectionalgorithm

Canny edge detection algorithm is one of the commonly used image processing tools. This algorithm provides good detection and localization of real edges while providing minimal response in low noise environments. The Canny edge detection algorithm consists of the following steps: (1) Reading the image for processing;(2) Noise reduction by filtering with Gaussian blurring filter;(3) Determining the gradients of the image to high regions with high spatial derivatives;(4) Relating the edge gradients to traceable detractions;(5) Tracing the valid edges where only the local maxima should be found as edges; and (6) Hysteresis thresholding to eliminate breaking up of edge contours.

Mathematical morphology opening algorithm [21,22]

Mathematical morphology was developed by Serra and Matheron. Mathematical morphology is most commonly applied to digital images. The basic idea of mathematical morphologyis to probe an image with a template shape, called the structuring element, to quantify the manner in which the structuring element fits within a given image. Opening and closing are two important operators from mathematical morphology. Both operators are derived from the fundamental operations of erosion and dilation. The basic effect of an opening operator is to remove some bright pixels from the edges of regions. An opening is defined as erosion followed by dilation using the same structuring element for both operations. Gray-level opening can similarly be used to select and preserve particular intensity patterns while attenuating others. Gray -level opening consists simply of gray-level erosion followed by gray-level dilation.

In grayscale morphology, images are functionsthat map a Euclidean space into □∪{∞, -∞}, where □ is the set of reals, ∞ is an element that is larger than any real number, and -∞ is an element smaller than any real number. Grayscale structuring elements are also functions of the same format known as structuring functions. Denoting an image by $f(x)$ and the structuring function by $b(x)$, the

[DOI: 10.18869/acadpub.ijrr.15.1.49]

gray-scale opening of f by b is given by $f_o b = (f! b) \oplus b$.

Median filter algorithm [23,24]

Median filtering is a nonlinear filtering method normally used to reduce noise in an image. Similar to the mean filter, the median filter considers each pixel in the image in turn and looks at neighbors to decide whether or not the image is representative of the surroundings. Instead of simply replacing the pixel values with the mean of neighborhood pixel values, median filter replaces the pixel values with the median of those values. The median value was calculated by first sorting all the pixel values from the surrounding neighborhood into numerical order, and then replacing the pixel being considered with the median pixel value. When the neighborhood under consideration contains an even number of pixels, the average of the two middle pixel values was used. Compared with the mean filter, the median filter has two main advantages. First, the median value is a more robust average than the mean; thus, a single very unrepresentative pixel in a neighborhood will not have a significant effect. Second, given that the median value must actually be the value of one of the pixels in the neighborhood, the median filter does not create new unrealistic pixel values when the filter straddles an edge. Therefore, the median filter is much better at preserving sharp edges than the mean filter. The whole process is completed in five steps as follows: (1) An appropriate template window size was selected. The template window slide in the image makes certain rules and overlaps the center of the template window and some image pixels. (2) Each pixel was read under the template window, and the gray values are obtained and listed in a row either from smallest to largest or vice versa. (3) The median of these values was obtained. (4) The central pixel was replaced from the window with the gray value. (5) Finally, the next successive overlapped window was selected, obtaining a column of new pixels from the right side and deleting a column of pixels from the left side. The first step was repeated for these pixels.

Diaphragm detection method

The diaphragm detection method consists of the following steps. (1) Patient images were extracted. The images of liver cancer patients were encoded to meet the needs of programming, which were acquired by Elekta Synergy-S linear accelerator system in the Motion-View™ XVI mode. (2) The detected range of diaphragm was selected. Given that the diaphragm was a non-rigid organization, normal respiratory motion may cause certain change in the shape of the diaphragm. The structure at the foot of the diaphragm is also relatively more complex; thus, deformation to the diaphragm foot was slightly larger than the other locations. However, considering the lack of a fixed reference point to another diaphragm location, detecting the same position of the diaphragm was difficult to repeat. Thus, the lowest point of the diaphragm was used to detect the diaphragmatic movement. The position of the diaphragm foot should also be included in the detected range (figure 1). (3) Classical edge detection operators were contrasted. Several classical edge detection operators were used to detect the selected image of the edge in the second step. Test results are shown in figure 2. Integrity and continuity of the edges in the image using Canny are better than those using other operators. (4) The selected image was enhanced and denoised using wavelet transform with Symlet4 of the wavelet toolbox in Matlab wavelet function. The image was then processed by binarization. (5) The curves of the patient's diaphragmatic movement were obtained by automatically detecting the location of the lowest point in the diaphragm.

Lipiodol detection method

The Lipiodoldetection method consists of the following steps. (1) Patient images were extracted. The image extraction method was the same as that described earlier. (2) Mathematical morphology opening operation is conducted. The entire extracted images are converted into grayscale. Mathematical morphology opening operations are also used in images with different radius of the flat disc-shaped structural

[DOI: 10.18869/acadpub.ijrr.15.1.49]

elements. (3) Background subtraction technique was performed. The images with mathematical morphology opening operation are used as background images to subtract the grayscale images. (4) The contrast of background subtraction images is adjusted and converted into a binary image. (5) Structure adhesions are removed. The structure connected to the lipiodol edge and lighter than the surrounding structure in the binary image was inhibited to extrude lipiodol. (6) The binary image of lipiodolis displayed. A clear display of the lipiodol binary image was obtained by filtering the image after the fifth step and processing using 2D median filtering algorithm, which is used as a stencil with an odd number of pixels. The image of lipiodol movement was then achieved by selecting the lipiodol motion range. (7)The curve of lipiodol movement is obtained. After lipiodol boundaries are sketched out, the coordinate position in the plane coordinate system of each pixel of lipiodol boundary was obtained. The lipiodolcentroid position was achieved by averaging the horizontal and vertical coordinates. Lipiodol centroid coordinate changes are recorded to obtain the curve of lipiodol movement. The outlines and centroids of lipiodol are shown in figure 3.

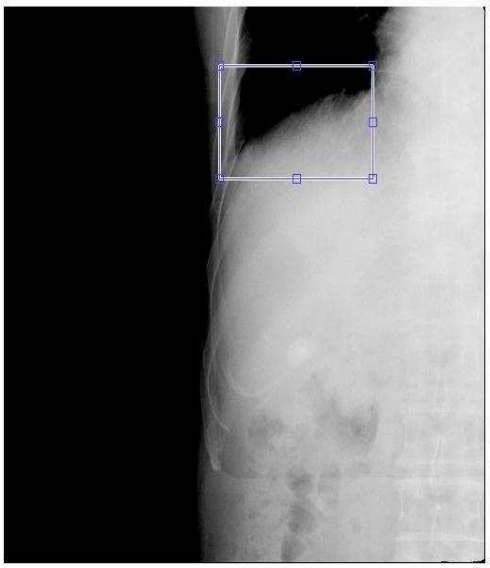

Figure 1. Diaphragm detection area.

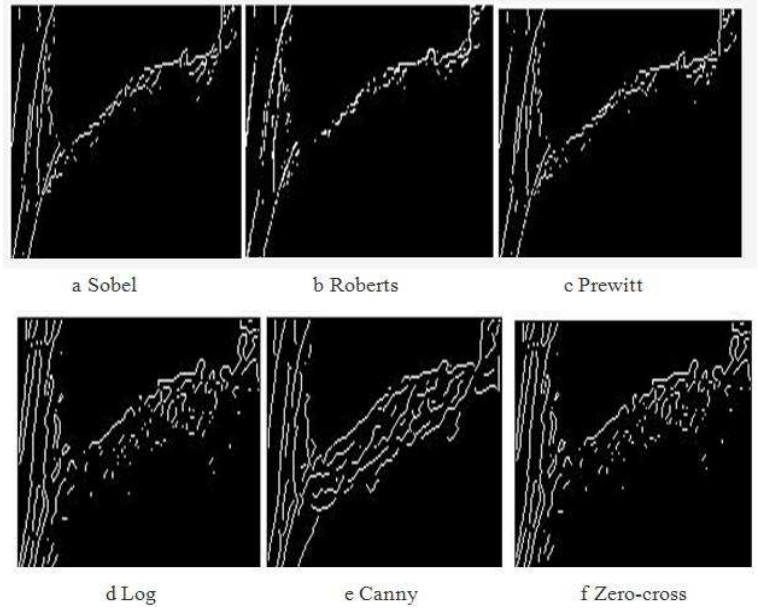

Figure 2. Different classical edge detection operators.

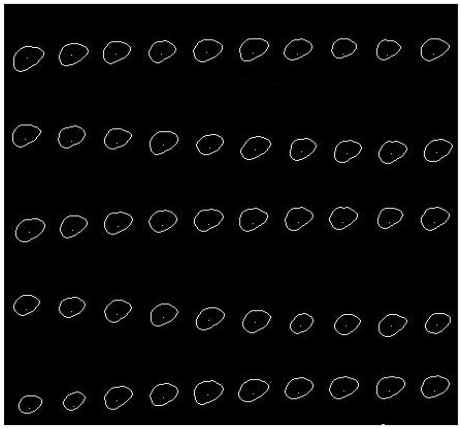

Figure 3. Outlines and centroids of lipiodol in the liver.

[DOI: 10.18869/acadpub.ijrr.15.1.49]

RESULTS

Detection of diaphragmatic motion

Comparison with manual measurements

After the lowest point of the diaphragm position of each image was determined manually, the approximate lipiodol center position was referred as the centroid position. First, the lipiodol centroid of arbitrarily one image can be used as a reference point. The lipiodol centroid positions of other images were also compared with the reference point. All differences in distance to obtain lipiodol motion curves were artificially connected. Manual measurement accuracy of the lowest point of the diaphragm was affected by many factors such as image resolution and pixel size. Therefore, the measurement accuracy was about ±0.5 mm (The measurement and comparison of all data were in free breathing condition). The average value of the three repeated measurements of the lowest point of the diaphragm was obtained as the manual measurement results. To avoid human error, all the diaphragm detection areas of patients' image were delineated by the same professional radiation physicist. The amplitude and cycle of the lowest point of the diaphragm foot were consistent with the manual measurement results (figure 4). Figure 4 shows the following: (1) Six to seven respiratory cycles are in XVI Motion-view™. The magnitude of the diaphragm movement is not exactly the same in the craniocaudal (CC) direction. The magnitude was about 6.7 mm to 8.0 mm with an average of 7.4 mm. (2) No lateral change of the diaphragm feet of the patients was detected in the lateral (LR) direction. Considering the impossibility of accurately manually measuring the movement of the diaphragm feet in the *y* direction, the manual measurement curve of the *LR* direction was not marked. (3) The lowest point of the detected diaphragm foot by programming did not completely coincide with that of the manual measurement. This finding is mainly attributed to the manual measurement that detected an error of about 0.5mm, which was significantly affected by image resolution and pixel size.

Diaphragmatic motion curves at different positions of same patient

The movement curves of the diaphragm feet, at one point in the middle of the diaphragm and another at the top, were detected (figure 5). Figure 5 shows the following: Three positions of diaphragmatic motion are very consistent. However, the closer diaphragm feet results in greater magnitude of diaphragm movement, and the closer the diaphragm top yields smaller magnitude of diaphragm movement. Given that more soft tissue structures are located at the diaphragm feet position, image grayscale changes are much more than those in the middle and upper positions of the diaphragm feet.

Curves of different fractions of diaphragm foot movement of same patient

Different diaphragm foot movement curves of same patient within five fractions in one week were contrasted to analyze the variation of respiratory movement. The curves of diaphragm movement in five treatment fractions (fraction 1 –fraction 5) are shown in Figure 6. In the state of calm breathing, the amplitude and period of the curves of fraction 1–fraction 5 are consistent (figure 6). However, when the patient was excited or coughed, the curve changed obviously (fraction 5).

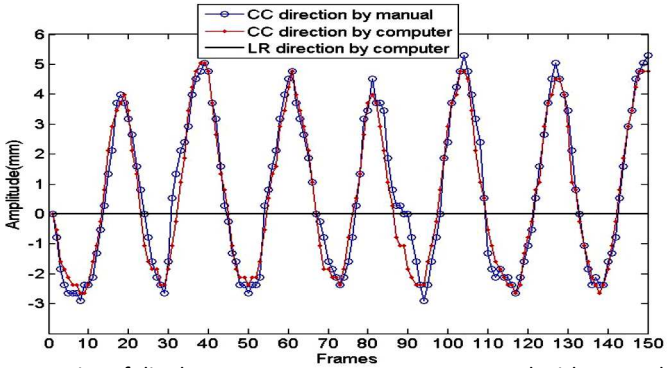

Figure 4. The lowest point of diaphragm movement curves compared with manual measurements.

[DOI: 10.18869/acadpub.ijrr.15.1.49]

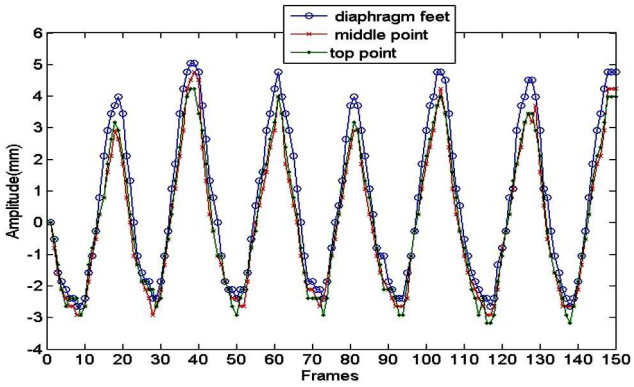

Figure 5. Curves of diaphragmatic motion at different diaphragm positions.

Curves of different fractions of diaphragm foot movement of same patient

Different diaphragm foot movement curves of same patient within five fractions in one week were contrasted to analyze the variation of respiratory movement. The curves of diaphragm movement in five treatment fractions (fraction 1 –fraction 5) are shown in Figure 6. In the state of calm breathing, the amplitude and period of the curves of fraction 1–fraction 5 are consistent (Figure 6). However, when the patient was excited or coughed, the curve changed obviously (fraction 5).

Detection of lipiodolmotion Compared with manual measurements

The lipiodol position of each image was visualized manually. The approximate lipiodol center was referred as the centroid position of the lipiodol centroid of any of the images can be used as a reference point. The centroid position of other images was also compared with the reference point, and artificially detected motion curve of lipiodol was constituted by the difference in distance. The manual measurement accuracy of lipiodol was also affected by many factors such as image resolution and pixel size. Accurate measurement of the movement curve of lipiodol in the LRdirection is also impossible by manual measurement, thereby not marked (figure7). figure 7 shows that : (1) Six to seven movement cycles are in XVI Motion-view™. The magnitude of lipiodol movement is not exactly the same as that in the *CC* direction. The magnitude ranged from 5.5mm to 7.0 mm with an average of 6.0 mm. (2) Compared with the CC direction, only slight changes were detected in the *LR* direction. The magnitude of diaphragm movement was not exactly the same as that in XVI Motion-view™. The magnitude ranged from 1.1mm to 1.6mm with an average of 1.3mm. (3) The point detected by programming did not completely coincide with the manual measurement result. This finding was mainly attributed to the manual measurement that detected an error of approximately 0.5mm, which was significantly affected by image resolution and pixel size.

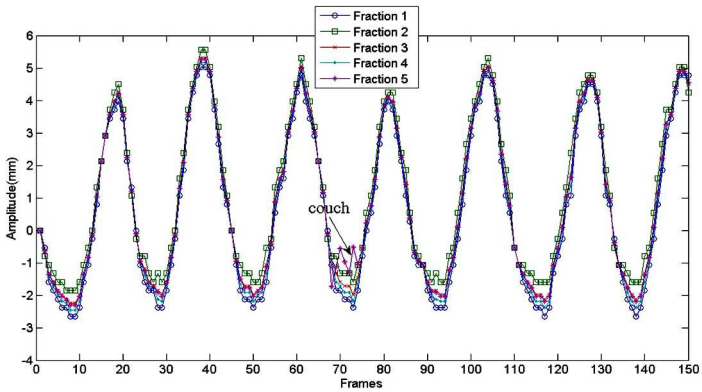

Figure 6. Curves of 5 different fractions in one week.

[DOI: 10.18869/acadpub.ijrr.15.1.49]

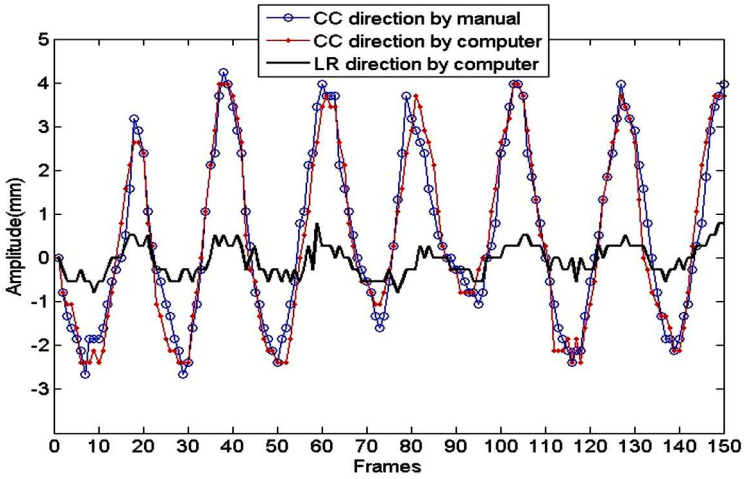

Figure 7. Lipiodol movement curves compared with manual measurements.

Curves of different fractions of lipiodol movement of same patient

The curves of lipiodol movement in five treatment fractions (fraction 1–fraction 5) in one week are shown in figure 8. Figure 8 shows that: (1) In calm breathing condition, the amplitude and period of the curves of fraction 1 –fraction 5 are consistent. However, when the patient is excited or has coughed, the curve obviously changes (fraction 5). (2) In the LRdirection, the curves of fraction 1–fraction 5 are not exactly the same, but the amplitude of the curves is about 1.5mm.

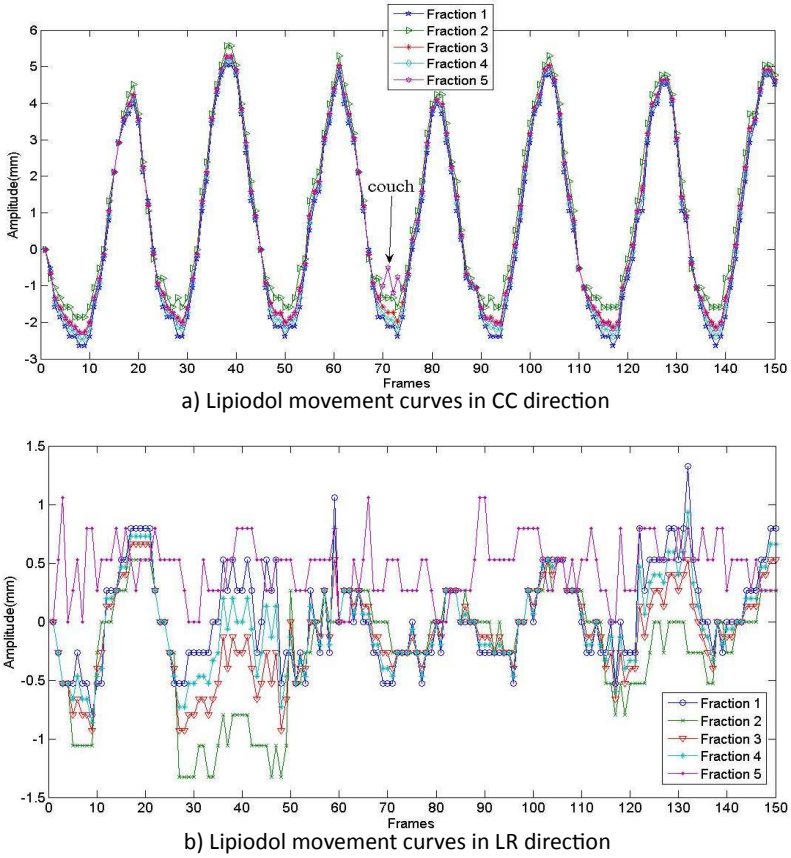

a) Lipiodol movement curves in CC direction

b) Lipiodol movement curves in LR direction

Figure 8. Curves of lipiodol movements of 5 different fractions in one week.

[DOI: 10.18869/acadpub.ijrr.15.1.49]

Curves of multiple lipiodolmovements of same patient

Multiplelipiodol points were found in images of some patients. Two obvious points were selected for detection. Two-point movement curves in the CC and LR directions are shown in figure 9. The movement of two points was basically the same as that in the CC direction, but certain difference is found in the LR direction. These findings are ascribed to two reasons. First, the pressure of two points coming from the abdominal organs was different. Second, when the liver shifts to a certain distance following respiratory movement, multiple lipiodolsmay overlap with the bone tissue, which would cause error. Fortunately, the error was about two pixels (0.5mm), which is acceptable in practice.

Contrastcurves of diaphragmatic and lipiodolmovement in same patient

Curves of manual measurement and computer detection of one patient's diaphragm and lipiodol movement are shown in Figure 10. In calm free breathing condition, the curve of diaphragm movement representing the respiration movement and the curve of lipiodol movement representing the tumor movement were both consistent with the movement cycle. The magnitudes of lipiodol movements detected manually and by computer were both slightly smaller than those of the diaphragm. This finding is mainly ascribed to the diaphragm, which was a soft tissue structure that produces a certain degree of deformation after extruded by the liver and other organs in the process of respiration. By contrast, lipiodol was a solid tissue structure that had slight distortion.

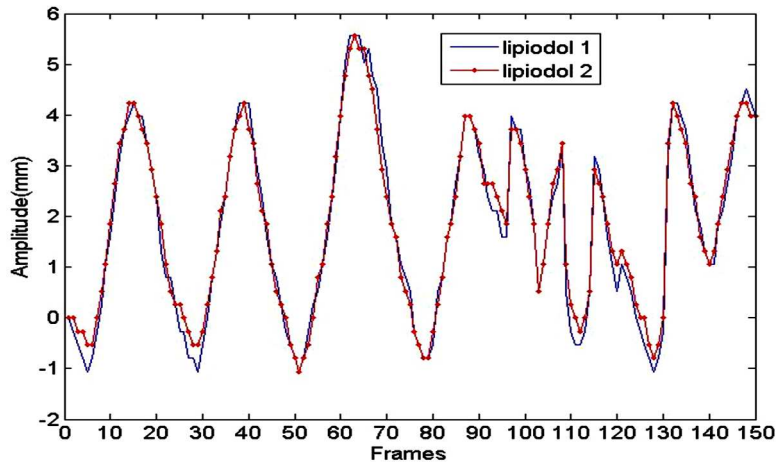

a) Lipiodol movement curves in CC direction

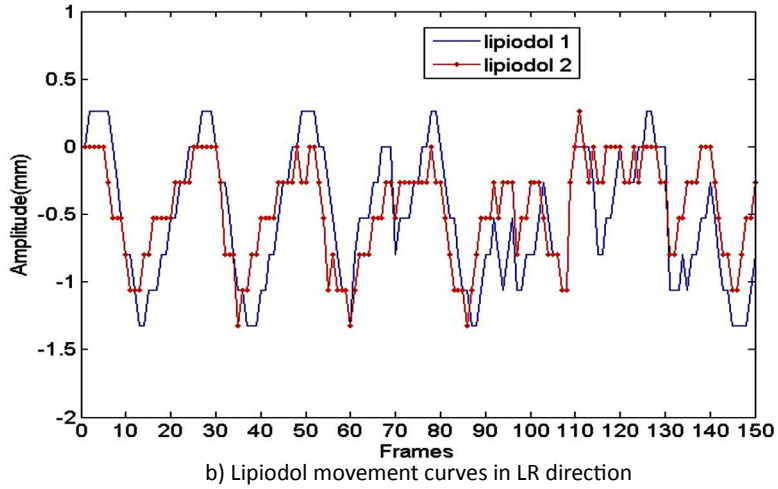

b) Lipiodol movement curves in LR direction

Figure 9. Two different lipiodol points in the same patient.

[DOI: 10.18869/acadpub.ijrr.15.1.49]

Curves of diaphragmatic movement by computer in different patients

To explore the laws of the patient's respiratory motion, it was used to study the differences of respiratory motion among the patients by comparing the diaphragmatic motion curves of different patients. The curves of diaphragmatic and lipiodolmovements in different patients are shown in figure 11.

In calm breathing condition, the amplitude and period of the curves of different patients (patient a– patient d) were significantly different. The magnitude of diaphragm movement ranged from 7mm to 10mm in the CC direction. The respiratory motion period of different patients ranged from 3s to 5s. At different points in time, the respiratory motion period and amplitude of the same patient in the data collection process was also not identical.

Curves of lipiodol movement by computer in different patients

The detected and compared lipiodol movement curves of four patients in the CC direction are shown in figure 12. In calm breathing condition, the lipiodol motion range of each patient caused by respiratory motion was not consistent. At different time points, the lipiodol motion amplitude of the same patient in the data collection process was also not identical, which was consistent with the diaphragmatic movement curves of different patients.

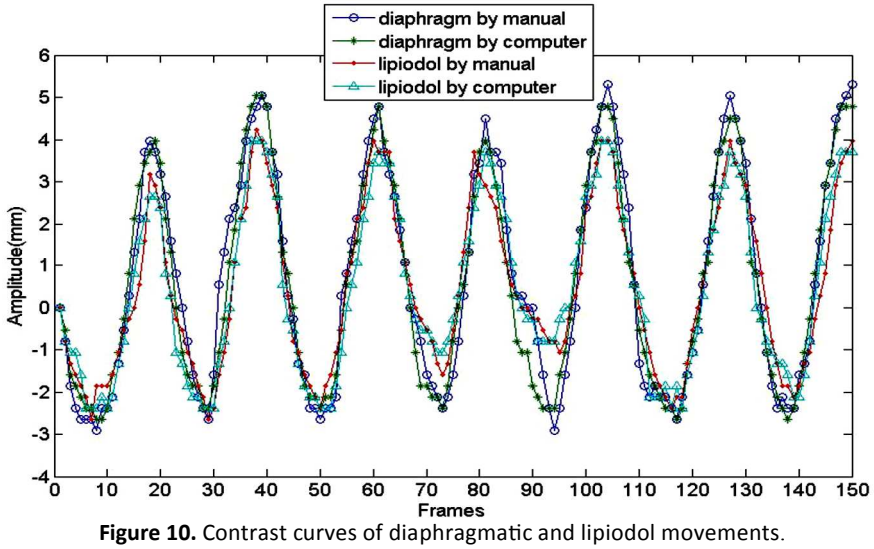

Figure 10. Contrast curves of diaphragmatic and lipiodol movements.

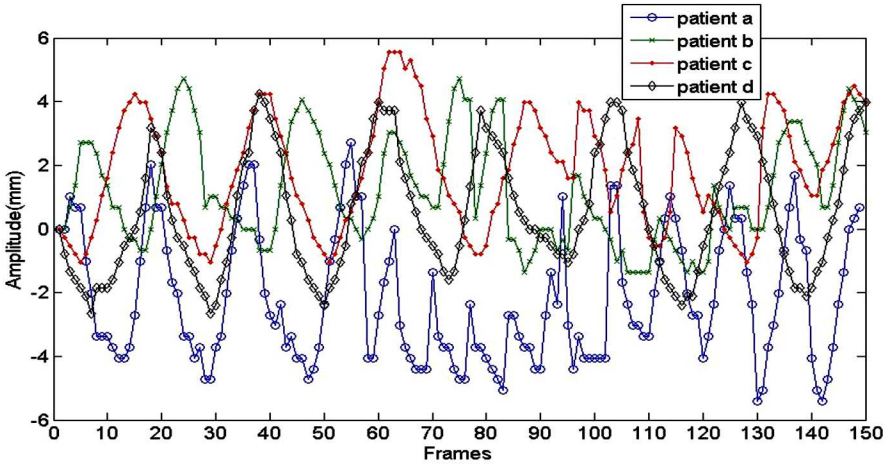

Figure 11. Diaphragmatic motion curves of 4 patients (patient a–patient d).

[DOI: 10.18869/acadpub.ijrr.15.1.49]

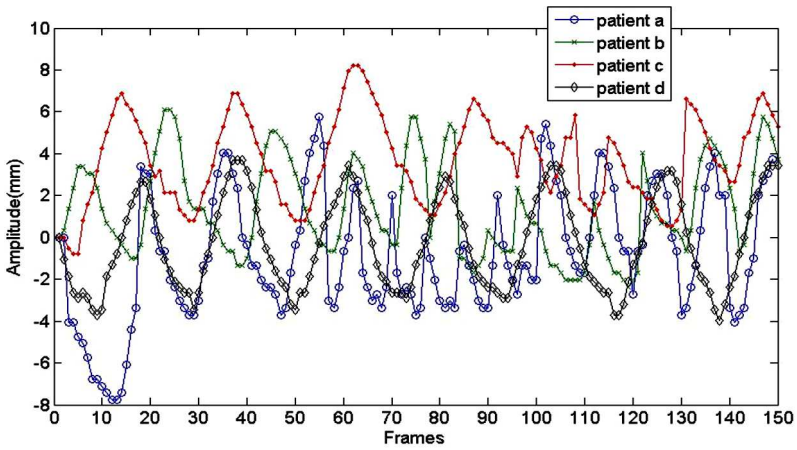

Figure 12. Lipiodol motion curves of 4 patients (patient a–patient d).

DISCUSSION

Radiation therapy has developed to an important treatment option that can extend survival and relieve symptoms in many tumor patients. It is very essential in radiation therapy to have accurate knowledge of the position and volume of the tumor in order to effectively apply sufficient radiation to the tumor while minimizing exposure to the surrounding normal tissue. Although many breath-hold and controlled breathing methods have been proposed, How to prevent or reduce tumors movement in the thoracic and abdominal is still a problem [25-28].

Tumors of the chest and abdomen were significantly affected by the patient's respiratory motion [29–30]. This finding is largely significant in improving the effect of radiotherapy and achieving precise radiotherapy by the patient's respiratory motion model. Diaphragmatic movement is caused by respiratory movement. Motion cycle and amplitude change of diaphragmatic movement with the respiratory movement have good consistency [31, 32]. In this study, we chose to study the patient's diaphragmatic movement instead of respiratory movement. The patient's respiratory movement model was achieved by tracking the diaphragmatic movement in fluoroscopy images. The curves of patient's diaphragmatic movement were obtained by wavelet transform and Canny edge detection method. Canny edge detection method has the following advantages: (1) the patient was in free breathing condition during treatment, without controlling breathing. Based on the patient image features, the motion of tumor was acquired from the motion of the diaphragm. (2) The respiratory trajectory was obtained by directly tracking the diaphragmatic movement. Therefore, the detection of respiratory movement is much more reliable than in vitro detecting methods. This tracking can also reflect the laws of human respiratory movement in time.

From the data, it reveals that the curves of the acquired diaphragmatic movement using the proposed method in this study agreed well with the manually marked reference locations in amplitude and period. From the results obtained it is clear that the curves of diaphragmatic motion had almost similar period and amplitude in one fraction. The respiratory period and amplitude of the same patient in different fractions had no significant differences; but the difference was obvious for different patients. The results showed that the proposed lipiodol detection methods in this study is correct which can effectively reflect the relevant rules of the tumor location caused by respiratory movement. Direct tracking of a liver tumor motion in fluoroscopic images is also feasible.

Six to seven respiratory cycles are found in a set of images. The magnitude and periods are not exactly the same in these cycles. Gierga *et al.* have measured the magnitude of tumor motion

[DOI: 10.18869/acadpub.ijrr.15.1.49]

for seven patients to be 7.4mm in the CC direction and 3.8mm in the AP direction [33]. Our results also found that the magnitude was an average of about 7.4mm in the CC direction which are in good agreement with Gierga. The results of this study showed there was no significant difference in the LR direction, the reason may be that the liver tumor movement is mainly in the CC direction. The respiratory cycle was no significantly different in different fractions of the same patient. The period and amplitude of respiratory movement were relatively stable. However, when the patient is excited or has coughed, the amplitude and cycle of respiratory movement would change significantly. These findings are in good agreement with the findings of other researchers reported in the literature.

In free calm breathing condition, liver tumor motion was significantly influenced by the respiratory movement. The diaphragmatic movement representing the respiratory movement and the lipiodol movement representing the tumor movement are in good agreement with the movement cycle. The cycles and magnitude of lipiodol movement are consistent in the same patient, but significantly different among different patients. The amplitude and period of the respiratory motion of different patients were significantly different. For different patients, uniform external boundary conditions should not be used to expand the tumor target. Individualized treatment plans should be developed, which was based on the characteristics of the patient's own breathing exercises.

CONCLUSIONS

In this study, we have demonstrated the feasibility of direct tracking liver tumor motion by mass or nearby anatomic feature in fluoroscope images. The automatic precise detection method was achieved by the proposed mathematical image processing technique. It can reflect the characteristics of respiratory and tumor motions. And also, it is shown that it can save much time and significantly improve measurement precision compared with manual measurement, which can be potentially used for the precise treatment of lung or liver cancer using either respiratory gating or beam tracking.

Conflict of interest: *Declared none.*

REFERENCES

1. Ekberg L, Holmberg O, Wittgren L, Bjelkengren G, Landberg T (1998) What margins should be added to the clinical target volume in radiotherapy treatment planning for lung cancer? *Radiat Oncol,* ***48:*** *71-77.*
2. Whitfield G A, Jackson A, Moore C, Price P (2008) Radical chemo-radiotherapy for adenocarcinoma of the distal esophagus and oesophagogastric junction: what planning margins should we use?. *British Journal of Radiology,* ***81:*** *921-934.* AffiliationsDepartment of Oncology, Malmoe University Hospital, S-205 02 Malmoe, SwedenCorresponding author.Affiliations
3. Department of Radiation Physics, Malmoe University Hospital, S-205 02 Malmoe, Sweden
4. van Baardwijk A, Bosmans G, Bentzen SM, Boersma L, Dekker A (2008) Radiation dose prescription for non-small-cell lung cancer according to normal tissue dose constraints: an in silico clinical trial. *Int J Radiat Oncol Biol Phys,* ***71:*** *1103–1110.*
5. Lin T ,Cerviño LI ,Tang X ,Vasconcelos N ,Jiang SB(2009) Fluoroscopic tumor tracking for image-guided lung cancer radiotherapy. *Phys Med Biol,* ***54:*** *981–992.*
6. Zhao B ,Yang Y ,Li T ,Li X ,Heron DE (2012) Dosimetric effect of intrafraction tumor motion in phase gated lung stereotactic body radiotherapy. *Med Phy,* ***39:*** *6629-6637.*
7. Rosenzweig K E, Hanley J, Mah D, Mageras G, Hunt M (2000) The deep inspiration breath-hold technique in the treatment of inoperable non–small-cell lung cancer. *Int. J Radiat Oncol Biol Phys,* ***48:*** *81-87.*
8. Mageras GS ,1Yorke E ,Rosenzweig K ,Braban L ,Keatley E (2001)Fluoroscopic evaluation of diaphragmatic motion reduction with a respiratory gated radiotherapy system. *Appl Clin Med Phys,* ***2:*** *191–200.*
9. Jiang Steve B(2006) Radiotherapy of mobile tumors. *Semin Radiat Oncol,* ***16:*** *239–248.*
10. Cervino LI, Jiang Y, Sandhu A, Jiang SB (2010) Tumor motion prediction with the diaphragm as a surrogate: a feasibility study. *Phys. Med. Biol,* ***55:*** *221-229.*
11. Shirato H ,1Harada T ,Harabayashi T, Hida K, Endo H (2003) Feasibility of insertion/implantation of 2.0-mm-diameter gold internal fiducial markers for precise setup and real-time tumor tracking in radiotherapy. *Int J Radiat Oncol Biol Phys,* ***56:*** *240–247.*
12. Tang X, Sharp G C and Jiang S B(2007) Fluoroscopic tracking of multiple implanted fiducial markers using multiple

[DOI: 10.18869/acadpub.ijrr.15.1.49]

object tracking. *Phys Med Biol,* ***52:*** *4081–4098.*

13. 1Ohta K ,Shimohira M ,Iwata H ,Hashizume T ,Ogino H) (2013Percutaneous fiducial marker placement under CT fluoroscopic guidance for stereotactic body radiotherapy of the lung: an initial experience. *J Radiat Res,* ***54:*** *957-961.*
14. Cui Y, Dy J G, Sharp G C, Alexander B and Jiang S B (2007) Robust fluoroscopic respiratory gating for lung cancer radiotherapy without implanted fiducial markers. *Phys Med Biol,* ***52:*** *741–755.*
15. Lewis JH ,Li R ,Watkins WT ,Lawson JD ,Segars WP) (2010Marker-less lung tumor tracking and trajectory reconstruction using rotational cone-beam projections: a feasibility study. *Phys Med Biol,* ***55:*** *2505-2522.*
16. Chen M and Siochi RA (2010) Diaphragm motion quantification in megavoltage cone-beam CT projection images. *Med Phys,* ***37:*** *2312-2320.*
17. Heuvel VD, Fugazzi J, Seppi E, Forman JD (2006) Clinical application of a repositioning scheme, using gold markers and electronic portal imaging. *Radiother Oncol,* ***79:*** *94-100.*
18. Li R and Sharp G (2013) Robust fluoroscopic tracking of fiducial markers: exploiting the spatial constraints. *Phys Med Biol,* ***58:*** *1789-1808.*
19. Wang TC and Karayiannis NB (1998) Detection of microcalcifications in digital mammograms using wavelets. *Medical Imaging, IEEE Transactions Info,* ***17:*** *498-509.*
20. Chan HP ,Vyborny CJ ,MacMahon H ,Metz CE ,Doi K) (1987Digital mammography: ROC studies of the effects of pixel size and unsharp-mask filtering on the detection of subtle micro-calcifications. *Invest Radiol,* ***22:*** *581-589.*
21. Hojjatoleslami A, Sardo L, Kittler J (1997) An RBF based classifier for the detection of microcalcifications in mammograms with outlier rejection capability. *Neural Networks, International Conference on IEEE,* ***3:*** *1379-1384.*
22. Jesús A and Jean S (2002) Automatic analysis of DNA microarray images using mathematical morphology. *Bioinformatics,* ***19:*** *553-556.*
23. Comer ML and Delp EJ (1999) Morphological operations for color image processing. *Journal of electronic imaging,* ***8:*** *279-289.*
24. Donoho DL (1995) De-noising by soft-thresholding. *IEEE Trans Info,* ***41:*** *613-627. .*
25. Horng SJ, Hsu LY, Li TR, Qiao SJ, Gong X (2013) Using Sorted Switching Median Filter to Remove High-Density Impulse Noises. *Journal of Visual Communication and Image Representation,* ***24:****956-967.*
26. Chang-li R, Yu-xin C, Lu-zhou W, Wu B, Qi-bin S (2015) The influence of respiratory motion on dose distribution of 3D-CRT and IMRT- A simulation study. *Int. J Radiat Res,* ***13:****39-44.*
27. Zehtabian M, Faghihi R, Mosleh-Shirazi MA, Shakibafard AR, Mohammadi M (2012) A fast model for prediction of respiratory lung motion for image-guided radiotherapy: A feasibility study. *Int. J Radiat Res,* ***10:*** *73-81.*
28. Xu Q, Hamilton RJ, Schowengerdt RA, Jiang SB (2007) A deformable lung tumor tracking method in fluoroscopic video using active shape models: a feasibility study. *Phys Med Biol,* ***52:*** *5277–5293.*
29. Xu Q, Hamilton RJ, Schowengerdt RA, Alexander B, Jiang SB (2008) Lung tumor tracking in fluoroscopic video based on optical flow. *Med Phys,* ***35:*** *5351–5359.*
30. Wagman R, Yorke E, Ford E, Giraud P, Mageras G (2003) Respiratory gating for liver tumors: use in dose escalation. *Int J Radiat Oncol Biol Phys,* ***55:*** *659-668.* Schmidt ML, Hoffmann L, Kandi M, Moller DS, Poulsen PR (2013) Dosimetric impact of respiratory motion, interfraction baseline shifts, and anatomical changes in radiotherapy of non-small cell lung cancer. *Acta Oncologica,* ***52:*** *1490-1496.*
31. Coolens C, Bracken J, Driscoll B, Hope A, Jaffray D (2012) Dynamic volume vs respiratory correlated 4D-CT for motion assessment in radiation therapy simulation. *Med Phys,* ***39:*** *2669-2681.*
32. Ford EC, Mageras GS, Yorke E, Rosenzweig, KE Wagman R (2002) Evaluation of respiratory movement during gated radiotherapy using film and electronic portal imaging. *Int J Radiat Oncol Biol Phys,* ***52:*** *522-531.*
33. Gierga DP, Brewer J, Sharp GC, Betke M, Willett M (2005) The correlation between internal and external markers for abdominal tumors: Implications for respiratory gating. *Int J Radiat Oncol Biol Phys,****61:*** *1551-1558.*

[DOI: 10.18869/acadpub.ijrr.15.1.49]